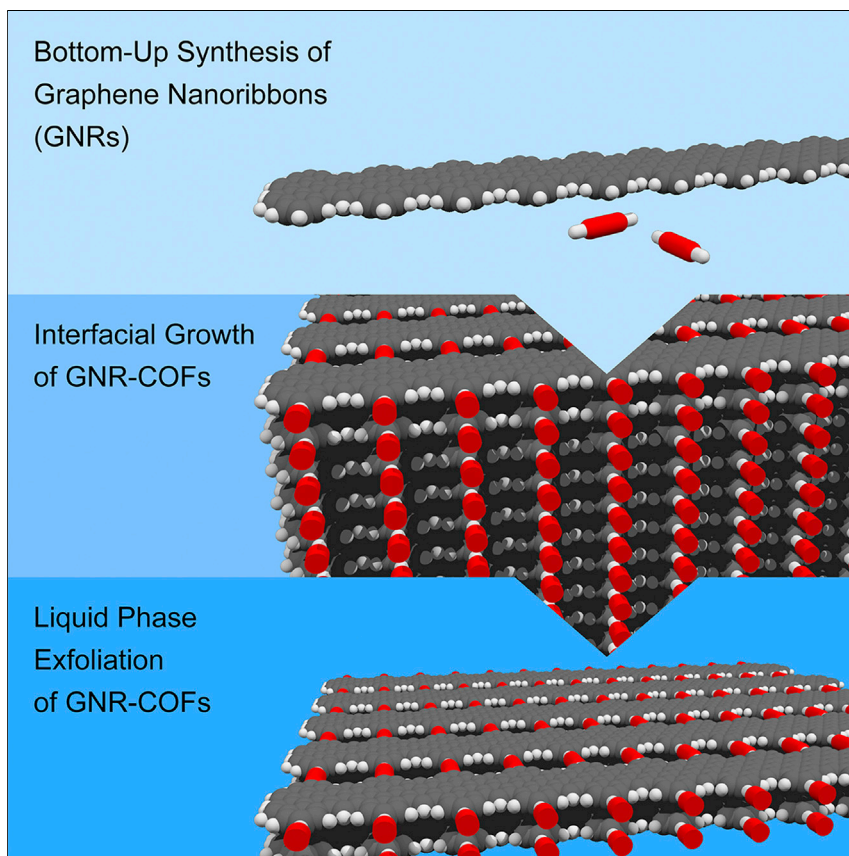


Article

Reticular Growth of Graphene Nanoribbon 2D Covalent Organic Frameworks



Fischer and co-workers present the realization of a porous crystalline two dimensional (2D) covalent organic framework (COF) grown from a polydisperse macromolecular building block. Bottom-up synthesized graphene nanoribbons (GNRs), quasi-one-dimensional (1D) atomically defined strips of single-layer graphene, self-assemble at a liquid-liquid interface into π -stacked 2D sheets cross-linked by diamine spacers. This distinct class of infinitely tunable 2D layered materials is anticipated to give rise to correlated phenomena emerging from the intrinsic anisotropy of constituent 1D GNR building blocks.

Gregory Veber, Christian S. Diercks, Cameron Rogers, ..., Chenhui Zhu, Jeffrey Bokor, Felix R. Fischer

ffischer@berkeley.edu

HIGHLIGHTS

A crystalline COF was grown from polydisperse 1D graphene nanoribbons (GNRs)

XRD reveals the intrinsic anisotropy of the 2D COF grown at a liquid-liquid interface

Crystalline domains of parallel GNRs enhance the bulk conductance in COF thin films

Multilayer 2D GNR-COF sheets can be delaminated to give access to few-layer GNR-COFs



Veber et al., Chem 6, 1125–1133
May 14, 2020 © 2020 Published by Elsevier Inc.
<https://doi.org/10.1016/j.chempr.2020.01.022>



Article

Reticular Growth of Graphene Nanoribbon
2D Covalent Organic Frameworks

Gregory Veber,¹ Christian S. Diercks,¹ Cameron Rogers,¹ Wade S. Perkins,¹ Jim Ciston,² Kyunghoon Lee,³ Juan Pablo Llinas,³ Alex Liebman-Peláez,⁴ Chenhui Zhu,⁴ Jeffrey Bokor,^{3,5} and Felix R. Fischer^{1,5,6,7,*}

SUMMARY

The reticular synthesis of covalent organic frameworks (COFs), extended porous two-dimensional (2D) or three-dimensional (3D) networks held together by strong, highly directional chemical bonds, has thus far been restricted to small, shape-persistent, molecular building blocks. Here, we demonstrate the growth of crystalline 2D COFs from a polydisperse macromolecule derived from single-layer graphene, bottom-up synthesized quasi-one-dimensional (1D) graphene nanoribbons (GNRs). X-ray scattering and transmission electron microscopy reveal that 2D sheets of GNR-COFs self-assembled at a liquid-liquid interface stack parallel to the layer boundary and exhibit an orthotropic crystal packing. Liquid-phase exfoliation of multilayer GNR-COF crystals gives access to large-area ($>10^5$ nm²) bilayer and trilayer cGNR-COF films. The functional integration of extended 1D materials into crystalline COFs greatly expands the structural complexity and the scope of mechanical and physical materials properties accessible through a deterministic reticular bottom-up approach.

INTRODUCTION

Covalent organic frameworks (COFs) are 2D or 3D extended periodic networks assembled from symmetric, shape-persistent molecular building blocks through strong, directional bonds.^{1,2} Traditional COF growth strategies heavily rely on reversible condensation reactions that guide the reticulation toward a desired thermodynamic equilibrium structure.³ The requirement for dynamic error correction, however, limits the choice of building blocks and thus the associated mechanical and electronic properties imbued within the periodic lattice of the COF. Furthermore, the poor electronic communication across imine and boronate ester linkers, most commonly used in the synthesis of 2D COFs, gives rise to semiconducting materials featuring large band gaps undesirable for advanced electronic applications.^{4,5} Charge-carrier transport in these materials is dominated by interlayer hopping mechanisms rather than through chemical bonds between linkers and the constituent molecular building blocks within a 2D sheet.⁶ Introduction of conjugated polymers as 1D conduction paths within a single COF sheet could address this shortcoming, yet the incorporation of macromolecules as building units in COFs has not been demonstrated. Recent advances in the bottom-up synthesis of graphene nanoribbons (GNRs), atomically thin quasi-1D strips of graphene, have inspired the development of a unique class of COF building blocks. The control over key structural parameters in GNRs, width,^{7–10} edge symmetry,^{7,11,12} dopant atom density,^{13–15} and dopant position^{16,17} gives rise to a highly tunable band structure and the emergence of exotic physical phenomena linked to symmetry protected topological states.^{18,19}

The Bigger Picture

Covalent organic frameworks (COFs) are a promising class of 2D materials for a variety of applications ranging from molecular sieves to organic electronics. Thus far the formation of these materials has been limited to discrete small molecule precursors utilized to reticulate the 2D or 3D networks. Here, we demonstrate the synthesis of a crystalline COF network derived from conductive 1D nanowires known as graphene nanoribbons (GNRs). Furthermore, we show that bilayer and trilayer GNR-COF films can be obtained via a liquid-phase exfoliation protocol. Now the chemical library for COF precursors has been expanded to include macromolecules and even carbon nanomaterials thus opening the opportunity to explore interesting materials properties emerging from polymer reticulation such as anisotropic charge transport and non-linear optoelectronic properties.



Here, we show that the exquisite structural control inherent to bottom-up synthesized GNRs can be adapted to introduce atomically precise spacings of functional groups along the edges of a ribbon, giving access to a shape-persistent quasi-1D macromolecular building block for the reticular synthesis of 2D COFs.

Imine linked GNR-COF films were assembled from aldehyde functionalized cGNRs (CHO-cGNR) and benzidine crosslinkers. Large area, homogeneous thin films of variable thickness were synthesized through interfacial polymerization at a liquid-liquid interface. By modulating the concentration of GNRs in the reaction mixture the film thickness can be controlled over a range of 2–22 nm. Fourier transform infrared (FT-IR) spectroscopy along with control experiments using unfunctionalized cGNRs confirmed that the GNR-COF films are covalently linked through imine bonds. The crystallographic structure of the GNR-COF was probed by using wide-angle X-ray scattering (WAXS) and transmission electron microscopy (TEM), revealing the extraordinary potential of reticular covalent self-assembly techniques to access densely packed parallel arrays of GNRs. Liquid-phase exfoliation of crystalline cGNR-COFs gives access to vertically stacked few-layered cGNR-COF flakes for applications in functional materials and advanced electronics.

RESULTS AND DISCUSSION

Synthesis and Characterization of CHO-cGNR

The synthesis of CHO-cGNRs is depicted in Figure 1A. Diels-Alder polymerization of acetal protected cyclopentadienone **3** yields the poly-phenylene precursor **4**. Size exclusion chromatography (SEC) shows a bimodal distribution of linear polymers ($M_n = 26,000 \text{ g mol}^{-1}$) and cyclic oligomers ($M_n = 3,000 \text{ g mol}^{-1}$) (Figure S1) characteristic for a step-growth polymerization mechanism.^{20,21} Acid catalyzed deprotection of crude **4** yields the aldehyde functionalized poly-phenylene **5**. Fractionation of the polymer mixture by preparative SEC gave access to samples of high molecular weight linear polymer **5** ($M_n = 18,500 \text{ g mol}^{-1}$) and low molecular weight cyclic oligomers ($M_n = 2,100 \text{ g mol}^{-1}$) (Figure 1B). MALDI mass spectroscopy of linear polymers **4** and **5** shows families of molecular ions separated by the repeat unit of the polymers, 676 g mol^{-1} and 588 g mol^{-1} for **4** and **5**, respectively (Figure 1C). The successful deprotection of **4** is further corroborated by the absence of characteristic peaks associated with the acetal protecting group ($\delta = 4.16\text{--}3.89 \text{ ppm}$) in $^1\text{H-NMR}$ spectra of **5** and the appearance of a new peak consistent with the aldehyde group hydrogen atoms ($\delta = 10.06\text{--}9.85 \text{ ppm}$) (Figure S2). Oxidative cyclodehydrogenation of **5** yields CHO-cGNR as a dark solid. Raman spectra of CHO-cGNRs show the characteristic signatures of cGNRs; a radial breathing like mode (RBLM) (253 cm^{-1}), the D ($1,332 \text{ cm}^{-1}$), and the G ($1,603 \text{ cm}^{-1}$) peaks as well as overtone 2D, D+D', and 2D' peaks (Figures 1D and S3).^{20,22,23} An overlay of the respective IR spectra of poly-phenylene **5** and CHO-cGNR confirms the presence of aldehyde groups in the GNRs. The relative intensity of the characteristic aldehyde C=O stretching mode at $1,699 \text{ cm}^{-1}$, with respect to the C=C stretching mode at $1,602 \text{ cm}^{-1}$, remains unchanged after the oxidative cyclodehydrogenation (Figure 1E). The UV-vis absorption spectrum of aldehyde functionalized CHO-cGNRs, indistinguishable from an original sample of cGNRs featuring solubilizing alkyl chains (Figure S4),²³ along with the characteristic Raman spectra (Figure 1D), is further evidence that the oxidative cyclodehydrogenation proceeds to the expected high degree of conversion.^{20,23}

Interfacial 2D cGNR-COF Growth

Imine cross-linked crystalline cGNR-COFs were grown by using a Lewis acid catalyzed interfacial polymerization.^{24–26} The physical separation of the catalyst ($\text{Sc}(\text{OTf})_3$), dissolved in an aqueous phase, and the organic building blocks, CHO-cGNRs and the benzidine cross-linker dispersed in an immiscible organic phase,

¹Department of Chemistry, University of California Berkeley, Berkeley, CA 94720, USA

²National Center for Electron Microscopy, Molecular Foundry, Lawrence Berkeley National Laboratory, Berkeley, CA 94720, USA

³Department of Electrical Engineering and Computer Sciences, University of California Berkeley, Berkeley, CA 94720, USA

⁴Advanced Light Source, Lawrence Berkeley National Laboratory, Berkeley, CA 94720, USA

⁵Materials Sciences Division, Lawrence Berkeley National Laboratory, Berkeley, CA 94720, USA

⁶Kavli Energy NanoSciences Institute at the University of California Berkeley and the Lawrence Berkeley National Laboratory, Berkeley, CA 94720, USA

⁷Lead Contact

*Correspondence: ffischer@berkeley.edu
<https://doi.org/10.1016/j.chempr.2020.01.022>

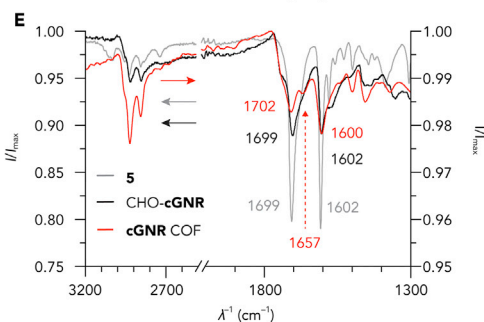
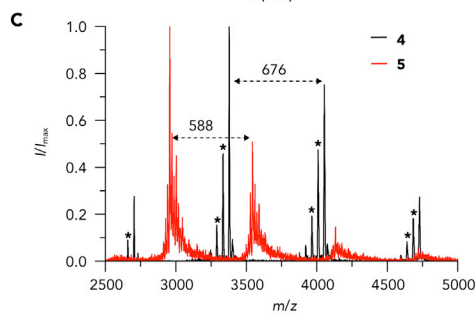
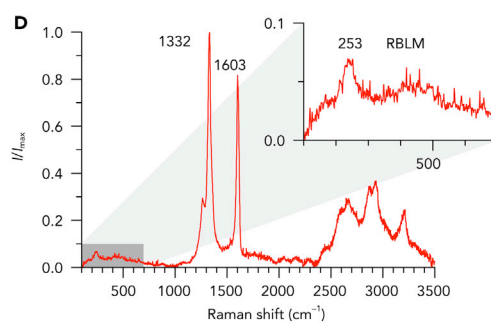
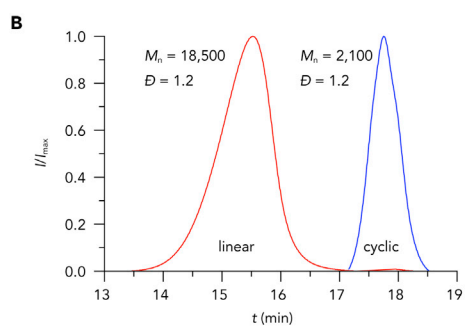
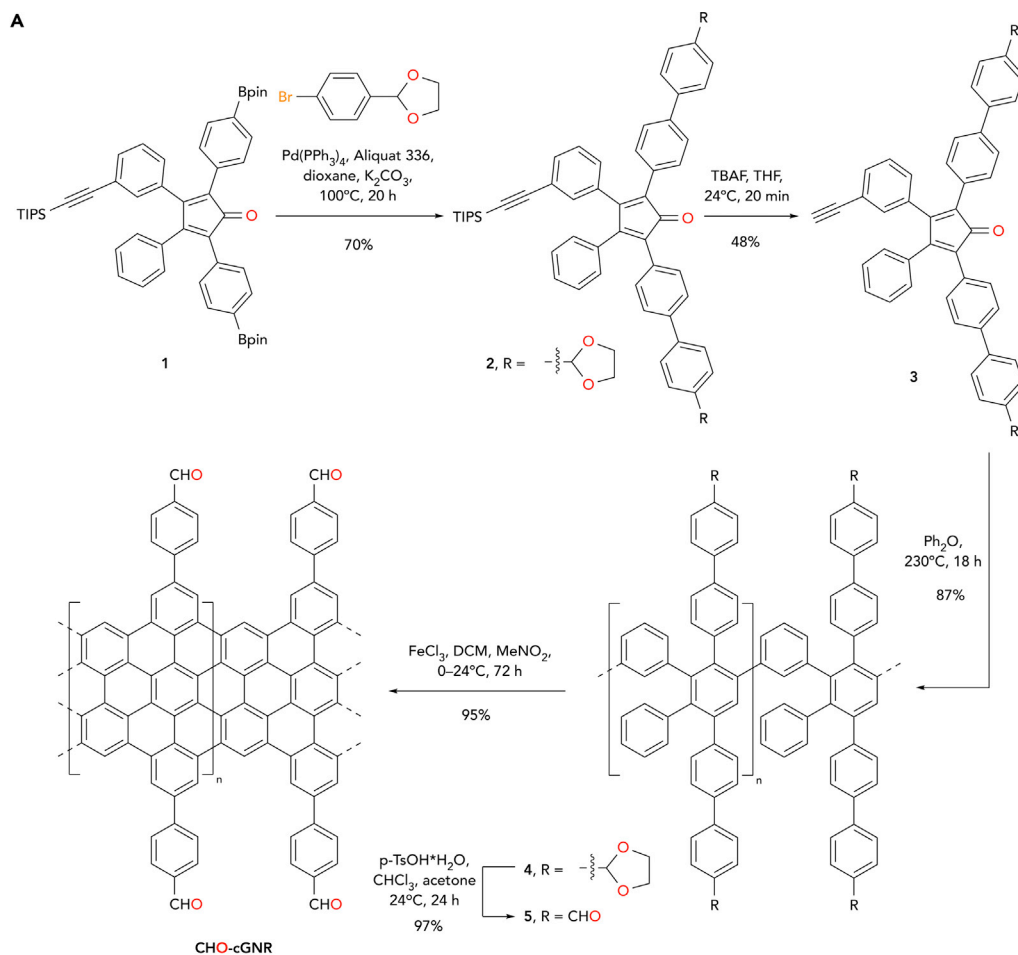


Figure 1. Synthesis and Characterization of Aldehyde Functionalized CHO-cGNRs

(A) Schematic representation of the synthesis of CHO-cGNR.

(B) SEC traces for the linear polymers (red) and cyclic oligomers (blue) of **5**.

(C) MALDI mass spectrum of crude **4** (black) and **5** (red) showing families of molecular ions separated by the mass of each polymer repeat unit (* corresponds to subfamilies of molecular ions resulting from the loss of acetal protecting groups).

(D) Raman spectrum ($\lambda_E = 532$ nm) of CHO-cGNRs. Inset shows the characteristic RBLM of cGNRs. See also Figure S3.

(E) FT-IR spectrum of **5** (gray), CHO-cGNRs (black), and cGNR-COF (red) showing the characteristic aldehyde C=O ($\lambda^{-1} = 1,699$ cm^{-1}) and aromatic C=C ($\lambda^{-1} = 1,602$ cm^{-1}) stretching modes in both **5** and CHO-cGNRs. The IR spectrum of cGNR-COF shows a decrease in the intensity of the aldehyde C=O ($\lambda^{-1} = 1,702$ cm^{-1}) relative to the C=C mode ($\lambda^{-1} = 1,600$ cm^{-1}) along with the signal for the C=N imine stretching mode ($\lambda^{-1} = 1,657$ cm^{-1}). See also Figure S7.

relegate the COF film growth exclusively to the liquid-liquid interface. The limited stability of dispersions of CHO-cGNRs in a wide variety of solvents along with the requirement that the density of the organic phase be greater than the aqueous phase to prevent the undesired precipitation of amorphous GNR aggregates at the liquid-liquid interface during film growth, narrowed the selection of organic solvents to mixtures of *o*-dichlorobenzene (*o*-DCB) and chloroform. High quality cGNR-COFs were obtained by layering an aqueous solution of Sc(OTf)₃ (5 mM) over a homogeneous dispersion of CHO-cGNRs and benzidine in *o*-DCB/CHCl₃ (*v/v* = 1:1). Over the course of 5–7 days gray films form at the liquid-liquid boundary that were scooped from the interface and transferred onto solid substrates (Figure 2A). A series of control experiments that alternately remove any one of the critical components, CHO-cGNRs, benzidine cross-linker, or Sc(OTf)₃, from the reaction mixture preclude the formation of cGNR-COFs even after extended reaction times. Similarly, the replacement of CHO-cGNRs with unfunctionalized cGNRs did not lead to the formation of COF films at the liquid-liquid interface (Figure S5). We, therefore, conclude that the observed cGNR-COF films formed in the presence of both reaction partners, CHO-cGNRs, benzidine, and the Lewis acid catalyst are not comprised of non-covalently assembled films formed at the interface solely driven by π - π interactions.

Optical microscopy of cGNR-COFs transferred onto a Si/SiO₂ surface reveal large flakes (>1,000 μm^2) of uniform color contrast (Figure 2B). Raman spectra recorded at various positions on cGNR-COF films show the characteristic RBLM, D, and G peaks associated with CHO-cGNRs, supporting the structural assignment (Figure 2C, blue and red traces). Areas of the SiO₂ apparently devoid of cGNR-COFs show only very weak Raman signatures (Figure 2C, black trace), attributed to small GNR aggregates or individual ribbons transferred with the solvent during the scooping process. Spatial Raman maps of the G-peak intensity of cGNR-COFs on Si/SiO₂ seamlessly coincide with the optical contrast in microscopy images (Figure S6). Attenuation of the FT-IR spectra recorded on transferred cGNR-COFs reveal the formation of imine bonds within the film. The FT-IR spectrum of the cGNR-COF, as compared with the CHO-cGNR, shows a decrease in the intensity of the characteristic aldehyde C=O stretching mode ($\lambda^{-1} = 1,702$ cm^{-1}) relative to the C=C mode ($\lambda^{-1} = 1,600$ cm^{-1}) (Figures 1E and S7). The imine C=N stretching mode resulting from the crosslinking of CHO-cGNRs with benzidine appears as a new shoulder at $\lambda^{-1} = 1,657$ cm^{-1} in the IR spectrum of cGNR-COFs (Figures 1E and S7).

cGNR-COF film morphology and thickness were examined by using scanning electron microscopy (SEM) and atomic force microscopy (AFM). SEM images of cGNR-COF films transferred onto TEM grids show large-scale homogeneity and well-defined film morphology (Figure 2D). Large areas (>100 μm^2) of homogeneous, smooth films show little to no amorphous regions or protrusions from the surface (Figure 2D). This is further supported by ambient AFM that shows films with height profiles ranging from 2–20 nm (Figures 2E and S8). The thickness of cGNR-COF films

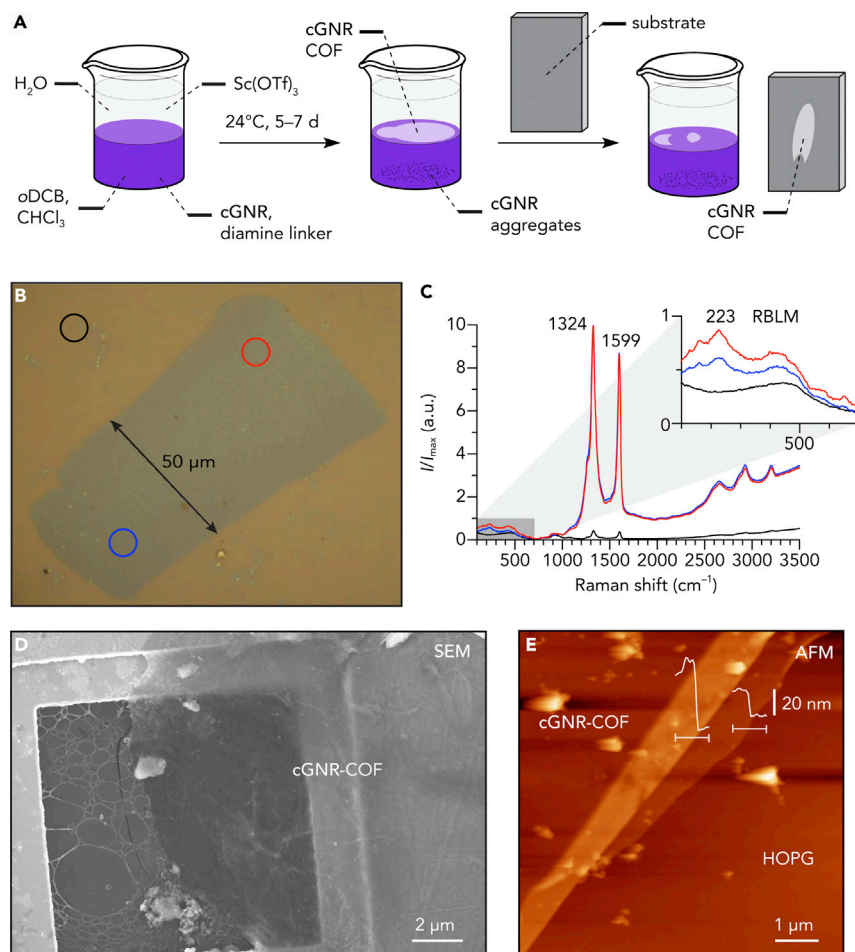


Figure 2. Synthesis and Characterization of cGNR-COF Thin Films

(A) Schematic representation of the interfacial polymerization and scooping transfer process.

(B) Optical microscopy image of a transferred cGNR-COF film on Si/SiO₂. Circles correspond to positions where Raman spectra were recorded. See also Figure S5.

(C) Raman spectra ($\lambda_E = 532$ nm) of the three regions highlighted in (B). Inset shows the characteristic RBLM. See also Figure S6.

(D) Scanning electron microscope image of cGNR-COF film dispersion dropcast onto a TEM grid (5 kV accelerating voltage).

(E) Atomic force microscopy (AFM) of ~20 nm cGNR-COF film on HOPG. Film thickness in folded regions corresponds to integer multiples of the single-layer film (~40 nm). See also Figure S8.

prepared through Lewis acid catalyzed growth at the liquid-liquid interface scales linearly with the initial concentration of CHO-cGNRs (Figure S9). Dilute dispersions of CHO-cGNRs ($67 \mu\text{g mL}^{-1}$) yield film thicknesses as low as 2 nm, whereas higher concentrations ($270 \mu\text{g mL}^{-1}$) form films with average thicknesses in excess of 20 nm.

We used synchrotron X-ray scattering to study the crystallographic structure of cGNR-COFs films. Figure 3A shows the projected trace of the wide-angle X-ray scattering (WAXS) pattern of powdered samples of cGNR-COFs grown at the liquid-liquid interface. The data were collected by suspending a dried, powdered sample of cGNR-COFs in a quartz capillary perpendicular to the incident beam. The WAXS pattern shows three characteristic reflections at $2\theta = 3.5^\circ$, 7.0° , and 12.0° corresponding to d-spacings of 2.5, 1.2, and 0.7 nm, respectively (Figure 3A). A structure model for the packing of cGNR-COF constructed in the triclinic space group $P\bar{1}$ with unit cell parameters

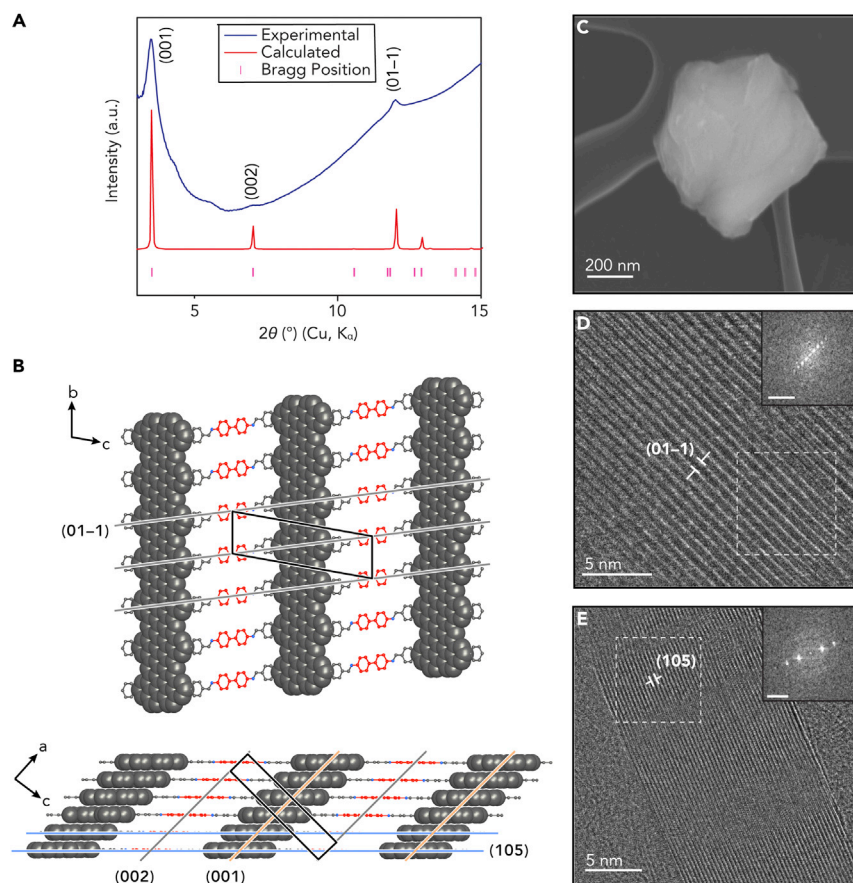


Figure 3. Powder X-ray Diffraction and HR-TEM of cGNR-COF Thin Films

(A) Experimentally and theoretically calculated WAXS pattern of powdered sample of cGNR-COF film.

(B) Structural model of cGNR-COF with unit cell (black box), orientation displaying lattice plane (01-1) corresponding to distance between linkers (0.7 nm) (top), orientation displaying interlayer packing and lattice planes (001) (orange), (002) (gray), and (105) (blue) corresponding to 2.5, 1.25, and 0.35 nm (bottom).

(C) Scanning electron microscope image of cGNR-COF film from HR-TEM sample.

(D) HR-TEM image of cGNR-COF crystallite displaying the (01-1) plane, fringes separated by 0.7 nm (white marker), Fourier diffractogram of the highlighted region (inset; scale bar, 5 nm^{-1}).

(E) HR-TEM image of cGNR-COF crystallite displaying the (105) plane, fringes represent π - π -stacking (0.35 nm) within the film, Fourier diffractogram of the highlighted region (inset; scale bar, 5 nm^{-1}).

$a = 5.0 \text{ \AA}$, $b = 7.4 \text{ \AA}$, $c = 25.5 \text{ \AA}$, $\alpha = 100^\circ$, $\beta = 90^\circ$, and $\gamma = 90^\circ$ is depicted in Figure 3B (Table S1). The predicted diffraction pattern is in good agreement with experimental data. The observed reflections at 2.5, 1.2, and 0.7 nm were assigned to the (001), (002), and (01-1) planes, respectively (Figure 3A). The (001) and (002) Bragg reflections correspond to the distance, and half the distance, between parallel ribbons (2.5 and 1.25 nm) whereas the (01-1) corresponds to the spacing of benzidine linkers (0.7 nm) lining the edges of the cGNRs (Figure 3B). The Bragg reflection associated with the interlayer π -stacking between cGNRs is masked by the pronounced background of the quartz capillary in the expected region of the WAXS pattern.

We used high-resolution transmission electron microscopy (HR-TEM) to study the crystalline domain size of cGNR-COF films directly scooped from the liquid-liquid

interphase (Figure 3C). The micrographs, recorded at a total electron dose of $100 \text{ e } \text{\AA}^{-2}$ to minimize sample damage, display clear lattice fringes corresponding to the distance between linkers (0.7 nm) (Figure 3D) and the π -stacking between ribbons (0.35 nm) (Figure 3E), respectively. The observed lattice fringes corroborate the molecular model depicted in Figure 3B and can be assigned to the (01–1) and (105) lattice planes, respectively. The fact that the (001) and (002) planes related to the distance between covalently linked cGNRs cannot be observed in the TEM images is attributed to a preferential orientation of the crystallites within the film relative to the TEM grid. After the scooping transfer the cGNR-COFs adopt orientations in which the lateral spacing between cGNRs (2.5 nm) lies on an axis perpendicular to the surface and remains out of focus leaving only the π -stacking and linker-linker distances to be observed by in-plane elastic scattering. Most notably, the HR-TEM demonstrates that the crystalline domain size ($>400 \text{ nm}^2$) is 1–2 orders of magnitude larger than previously reported solution processable GNR films formed via π -stacking alone.²⁷ cGNR-COFs not only self-assemble into larger crystallites but macromolecular reticulation through directional covalent bonds allows for the rational design of highly anisotropic materials.

Electrical Conductance of Multilayered cGNR-COF Films

Next, we explored the electrical conductance within the crystalline domains in cGNR-COF films. Large-area thick ($>10 \text{ nm}$) cGNR-COF films were directly scooped from the liquid-liquid interface onto Al_2O_3 substrates prepatterned with Pt electrodes. Figure S10 shows a representative optical microscopy image of a large ($>10^4 \text{ }\mu\text{m}^2$) cGNR-COF film bridging the gap between multiple prepatterned electrodes. Even in the absence of a gate bias ($V_g = 0 \text{ V}$) cGNR-COF devices exhibit drain currents (I_{ds}) as large as 2 nA at very low source-drain bias ($V_{ds} = 10 \text{ V}$) when compared with dropcast π -stacked GNR thin films.²⁷ These initial I - V characteristics suggest that the presence of crystalline domains within these multilayered cGNR-COF films contribute to an enhancement of the bulk conductivity across sizable areas of the film.

Liquid-Phase Exfoliation of cGNR-COF Films

Finally, adopting a liquid-phase exfoliation protocol for the delamination of crystalline 2D COFs, we were able to access free-standing few-layer 2D cGNR-COF sheets. A dispersion of multilayer films grown from a saturated CHO-cGNR solution in acetone was transferred to *o*-DCB, sonicated, and dropcast onto Si/SiO₂. The resulting cGNR-COF flakes were analyzed using ambient AFM to determine the film thickness, size, and homogeneity (Figures 4A and 4B). The lateral dimensions of the cGNR-COF flakes are $>10^5 \text{ nm}^2$ and range in thickness between 0.70 nm (Figure 4C) and 1.05 nm (Figure 4D), corresponding to bilayer and trilayer stacks of 2D cGNR-COF sheets (π - π -stacking distance $\Delta = 0.35 \text{ nm}$). Some exfoliated films exhibit layered height profiles commensurate with step-edges within a single flake (Figure S11).

The orthotropic crystal packing adopted by GNRs in 2D COF films represents a unique opportunity to enhance the chemical, physical, and optoelectronic properties of COFs by independently tuning the mechanical and electrical material properties along all three axes of the crystal lattice. The simplicity of our interfacial GNR-COF growth and liquid-phase exfoliation protocol opens the path to accessing densely packed 2D sheets of parallel GNRs for high-performance electronic device architectures and the exploration of exotic physical phenomena emerging from deterministically engineered stacks of anisotropic layered 2D materials.

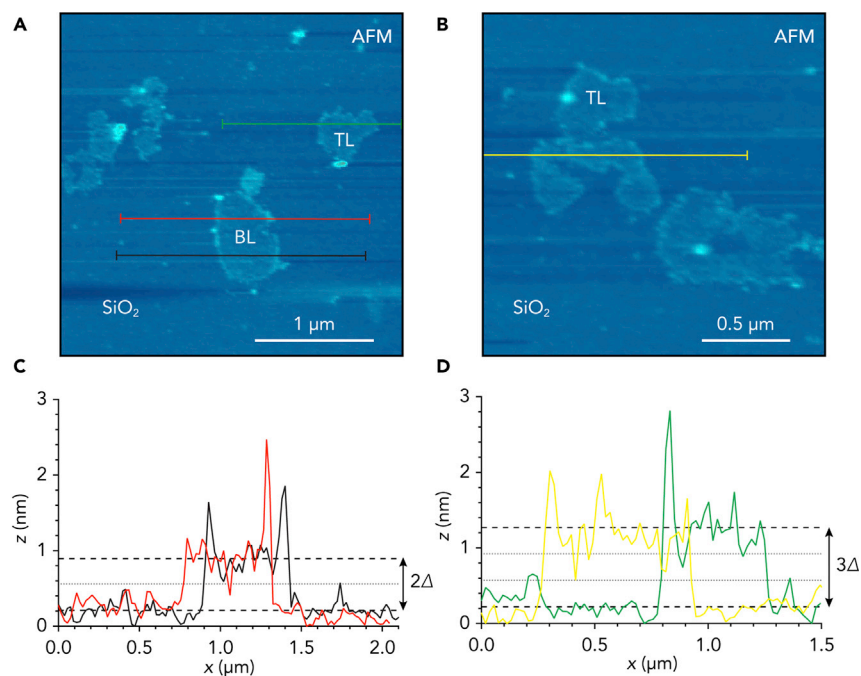


Figure 4. Chemically Exfoliated Bilayer and Trilayer cGNR-COF Flakes on SiO₂ Substrates

(A) AFM topographic images of liquid-phase exfoliated cGNR-COF on SiO₂.

(B) AFM topographic images of liquid-phase exfoliated cGNR-COF on SiO₂.

(C) AFM z-height profiles along the lines depicted in (A). Averaged background and averaged plateau height (black dashed lines), spacing corresponding to interlayer π - π -stacking distance ($\Delta = 0.35$ nm) as determined via HR-TEM and diffraction models (gray dotted lines). See also Figure S11.

(D) AFM z-height profiles along the lines depicted in (B). Averaged background and averaged plateau height (black dashed lines), spacing corresponding to interlayer π - π -stacking distance ($\Delta = 0.35$ nm) as determined via HR-TEM, and diffraction models (gray dotted lines).

EXPERIMENTAL PROCEDURES

All experimental details are presented in the [Supplemental Information](#).

SUPPLEMENTAL INFORMATION

Supplemental Information can be found online at <https://doi.org/10.1016/j.chempr.2020.01.022>.

ACKNOWLEDGMENTS

Research supported by the Office of Naval Research MURI program N00014-16-1-2921 (molecular synthesis, characterization, and COF film growth) and the Center for Energy Efficient Electronics NSF award 0939514 (GNR synthesis and characterization); research used beamline 7.3.3 of the Advanced Light Source, which is a DOE Office of Science User Facility under contract no. DE-AC02-05CH11231 (WAXS); and work at the Molecular Foundry (NCEM) was supported by the Office of Science and Office of Basic Energy Sciences of the U.S. Department of Energy under contract no. DE-AC02-05CH11231 (TEM). Berkeley NMR Facility is supported in part by NIH grants 1S10RR016634-01, SRR023679A, and S10OD024998.

AUTHOR CONTRIBUTIONS

G.V. and F.R.F. conceived the experiments. G.V. performed synthesis, COF growth, sample preparation, characterization, and data analysis. G.V. and C.R. performed

SEM. G.V. and W.S.P. performed ambient AFM. C.Z. and A.L.-P. performed X-ray diffraction. C.S.D. performed diffraction data analysis and modeling. J.C. performed TEM. K.L. and J.P.L. performed electrical conductivity measurements. G.V., C.S.D., and F.R.F. contributed to writing of the paper.

DECLARATION OF INTERESTS

The authors declare no competing interests.

Received: October 7, 2019

Revised: November 14, 2019

Accepted: January 30, 2020

Published: February 24, 2020

REFERENCES

- Diercks, C.S., and Yaghi, O.M. (2017). The atom, the molecule, and the covalent organic framework. *Science* 355, 6328.
- Colson, J.W., and Dichtel, W.R. (2013). Rationally synthesized two-dimensional polymers. *Nat. Chem.* 5, 453–465.
- Smith, B.J., Overholts, A.C., Hwang, N., and Dichtel, W.R. (2016). Insight into the crystallization of amorphous imine-linked polymer networks to 2D covalent organic frameworks. *Chem. Commun. (Camb.)* 52, 3690–3693.
- Joshi, T., Chen, C., Li, H., Diercks, C.S., Wang, G., Waller, P.J., Li, H., Bredas, J.L., Yaghi, O.M., and Crommie, M.F. (2019). Local electronic structure of molecular heterojunctions in a single-layer 2D covalent organic framework. *Adv. Mater.* 31, e1805941.
- Chen, C., Joshi, T., Li, H., Chavez, A.D., Pedramrazi, Z., Liu, P.N., Li, H., Dichtel, W.R., Bredas, J.L., and Crommie, M.F. (2018). Local electronic structure of a single-layer porphyrin-containing covalent organic framework. *ACS Nano* 12, 385–391.
- Dogru, M., and Bein, T. (2014). On the road towards electroactive covalent organic frameworks. *Chem. Commun. (Camb.)* 50, 5531–5546.
- Cai, J., Ruffieux, P., Jaafar, R., Bieri, M., Braun, T., Blankenburg, S., Muoth, M., Seitsonen, A.P., Saleh, M., Feng, X., et al. (2010). Atomically precise bottom-up fabrication of graphene nanoribbons. *Nature* 466, 470–473.
- Chen, Y.C., De Oteyza, D.G., Pedramrazi, Z., Chen, C., Fischer, F.R., and Crommie, M.F. (2013). Tuning the band gap of graphene nanoribbons synthesized from molecular precursors. *ACS Nano* 7, 6123–6128.
- Talirz, L., Söde, H., Dumschlaff, T., Wang, S., Sanchez-Valencia, J.R., Liu, J., Shinde, P., Pignedoli, C.A., Liang, L., Meunier, V., et al. (2017). On-surface synthesis and characterization of 9-atom wide armchair graphene nanoribbons. *ACS Nano* 11, 1380–1388.
- Zhang, H., Lin, H., Sun, K., Chen, L., Zagranjarski, Y., Aghdassi, N., Duhm, S., Li, Q., Zhong, D., Li, Y., et al. (2015). On-surface synthesis of rylene-type graphene nanoribbons. *J. Am. Chem. Soc.* 137, 4022–4025.
- Liu, J., Li, B.W., Tan, Y.Z., Giannakopoulos, A., Sanchez-Sanchez, C., Beljonne, D., Ruffieux, P., Fasel, R., Feng, X., and Müllen, K. (2015). Toward cove-edged low band gap graphene nanoribbons. *J. Am. Chem. Soc.* 137, 6097–6103.
- Ruffieux, P., Wang, S., Yang, B., Sánchez-Sánchez, C., Liu, J., Dienel, T., Talirz, L., Shinde, P., Pignedoli, C.A., Passerone, D., et al. (2016). On-surface synthesis of graphene nanoribbons with zigzag edge topology. *Nature* 531, 489–492.
- Cai, J., Pignedoli, C.A., Talirz, L., Ruffieux, P., Söde, H., Liang, L., Meunier, V., Berger, R., Li, R., Feng, X., et al. (2014). Graphene nanoribbon heterojunctions. *Nat. Nanotechnol.* 9, 896–900.
- Bronner, C., Strelau, S., Gille, M., Brauße, F., Haase, A., Hecht, S., and Tegeder, P. (2013). Aligning the band gap of graphene nanoribbons by monomer doping. *Angew. Chem. Int. Ed. Engl.* 52, 4422–4425.
- Zhang, Y., Zhang, Y., Li, G., Lu, J., Lin, X., Du, S., Berger, R., Feng, X., Müllen, K., and Gao, H.J. (2014). Direct visualization of atomically precise nitrogen-doped graphene nanoribbons. *Appl. Phys. Lett.* 105.
- Cloke, R.R., Marangoni, T., Nguyen, G.D., Joshi, T., Rizzo, D.J., Bronner, C., Cao, T., Louie, S.G., Crommie, M.F., and Fischer, F.R. (2015). Site-specific substitutional boron doping of semiconducting armchair graphene nanoribbons. *J. Am. Chem. Soc.* 137, 8872–8875.
- Durr, R.A., Haberler, D., Lee, Y.L., Blackwell, R., Kalayjian, A.M., Marangoni, T., Ihm, J., Louie, S.G., and Fischer, F.R. (2018). Orbitally matched edge-doping in graphene nanoribbons. *J. Am. Chem. Soc.* 140, 807–813.
- Rizzo, D.J., Veber, G., Cao, T., Bronner, C., Chen, T., Zhao, F., Rodriguez, H., Louie, S.G., Crommie, M.F., and Fischer, F.R. (2018). Topological band engineering of graphene nanoribbons. *Nature* 560, 204–208.
- Gröning, O., Wang, S., Yao, X., Pignedoli, C.A., Borin Barin, G., Daniels, C., Cupo, A., Meunier, V., Feng, X., Narita, A., et al. (2018). Engineering of robust topological quantum phases in graphene nanoribbons. *Nature* 560, 209–213.
- Narita, A., Feng, X., Hernandez, Y., Jensen, S.A., Bonn, M., Yang, H., Verzhbitskiy, I.A., Casiraghi, C., Hansen, M.R., Koch, A.H., et al. (2014). Synthesis of structurally well-defined and liquid-phase-processable graphene nanoribbons. *Nat. Chem.* 6, 126–132.
- Narita, A., Verzhbitskiy, I.A., Frederickx, W., Mali, K.S., Jensen, S.A., Hansen, M.R., Bonn, M., De Feyter, S., Casiraghi, C., Feng, X., and Müllen, K. (2014). Bottom-up synthesis of liquid-phase-processable graphene nanoribbons with near-infrared absorption. *ACS Nano* 8, 11622–11630.
- Joshi, D., Hauser, M., Veber, G., Berl, A., Xu, K., and Fischer, F.R. (2018). Super-resolution imaging of clickable graphene nanoribbons decorated with fluorescent dyes. *J. Am. Chem. Soc.* 140, 9574–9580.
- Perkins, W., and Fischer, F.R. (2017). Inserting porphyrin quantum dots in bottom-up synthesized graphene nanoribbons. *Chemistry* 23, 17687–17691.
- Matsumoto, M., Valentino, L., Stiehl, G.M., Balch, H.B., Corcos, A.R., Wang, F., Ralph, D.C., Mariñas, B.J., and Dichtel, W.R. (2018). Lewis-acid-catalyzed interfacial polymerization of covalent organic framework films. *Chem* 4, 308–317.
- Sahabudeen, H., Qi, H., Glatz, B.A., Tranca, D., Dong, R., Hou, Y., Zhang, T., Kuttner, C., Lehnert, T., Seifert, G., et al. (2016). Wafer-sized multifunctional polyimine-based two-dimensional conjugated polymers with high mechanical stiffness. *Nat. Commun.* 7, 13461.
- Dai, W., Shao, F., Szczerbiński, J., McCaffrey, R., Zenobi, R., Jin, Y., Schlüter, A.D., and Zhang, W. (2016). Synthesis of a two-dimensional covalent organic monolayer through dynamic imine chemistry at the air/water interface. *Angew. Chem. Int. Ed. Engl.* 55, 213–217.
- Shekhirev, M., Vo, T.H., Pour, M.M., Lipatov, A., Munukutla, S., Lyding, J.W., and Sinitskii, A. (2017). Interfacial self-assembly of atomically precise graphene nanoribbons into uniform thin films for electronics applications. *ACS Appl. Mater. Interfaces* 9, 693–700.

Chem, Volume 6

Supplemental Information

Reticular Growth of Graphene Nanoribbon

2D Covalent Organic Frameworks

Gregory Veber, Christian S. Diercks, Cameron Rogers, Wade S. Perkins, Jim Ciston, Kyunghoon Lee, Juan Pablo Llinas, Alex Liebman-Peláez, Chenhui Zhu, Jeffrey Bokor, and Felix R. Fischer

I. Supplemental Data Items

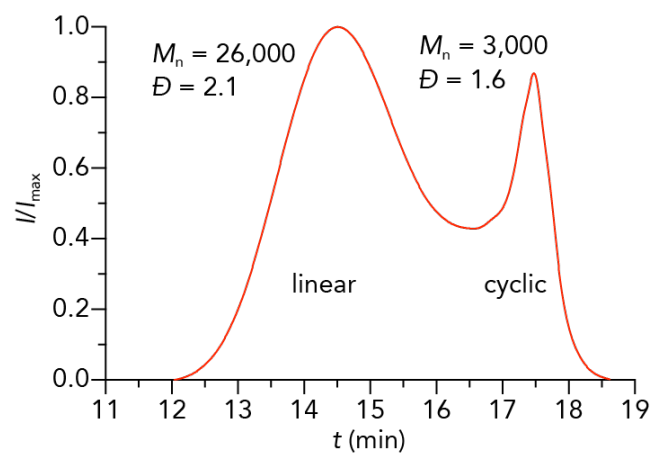


Figure S1. Size Exclusion Chromatography Characterization of Crude Poly-phenylene 4
SEC trace (CHCl_3) of crude poly-phenylene **4** containing linear polymers and cyclic oligomers.

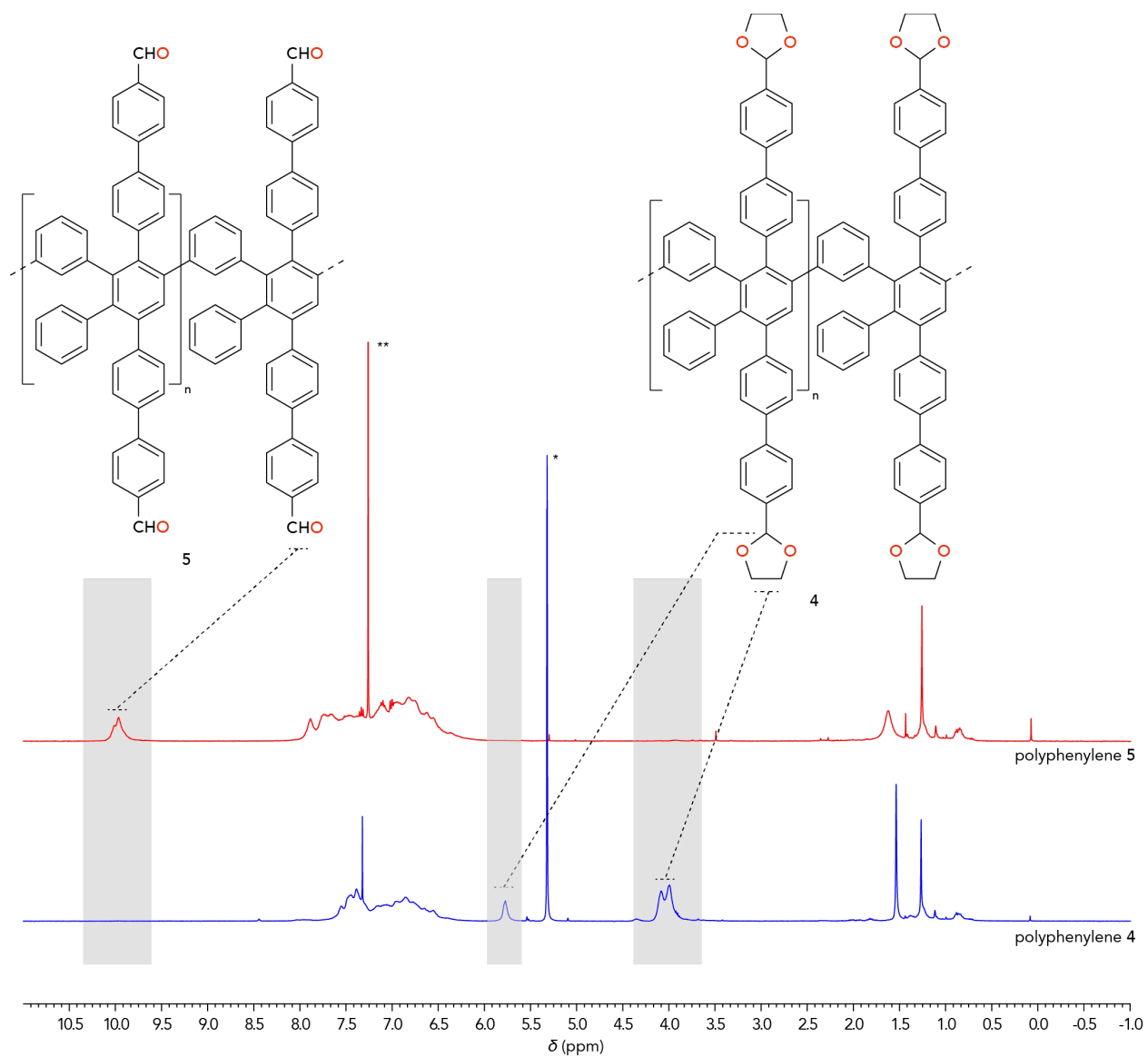


Figure S2. NMR Characterization of Poly-phenylene 4 and Poly-phenylene 5

¹H-NMR (400 MHz, CD₂Cl₂) of poly-phenylene **4** (blue), and ¹H-NMR (400 MHz, CDCl₃) of poly-phenylene **5** (red) following deprotection of the acetal groups. (* residual CH₂Cl₂, ** residual CHCl₃)

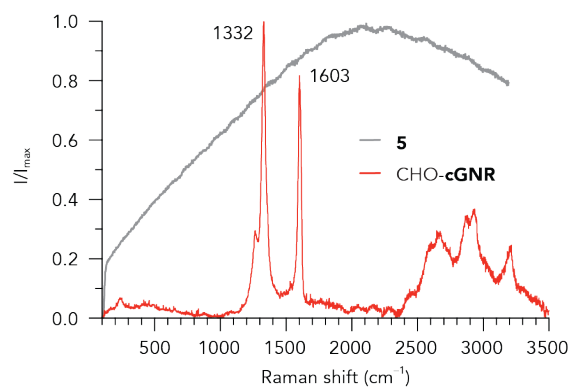


Figure S3. Raman Spectroscopy of CHO-cGNRs and Poly-phenylene 5, related to Figure 1D
Raman spectrum ($\lambda_E = 532$ nm) of CHO-cGNRs (red) and poly-phenylene 5 (gray).

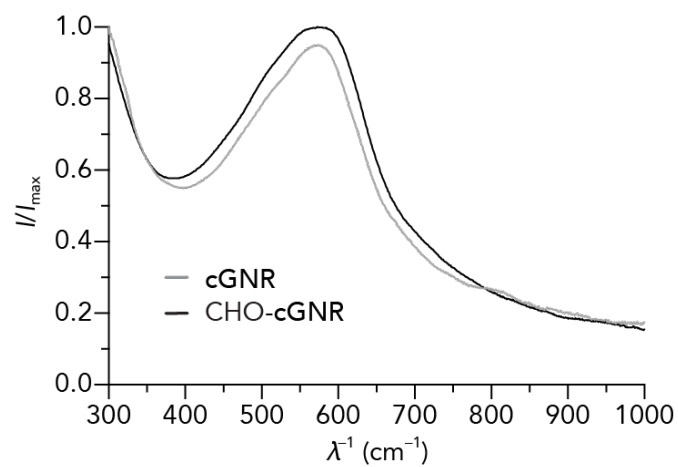


Figure S4. UV/vis Spectrum of cGNRs and CHO-cGNRs

UV/vis absorption spectrum of unfunctionalized cGNR and CHO-cGNR dispersions in N-methylpyrrolidone (NMP).

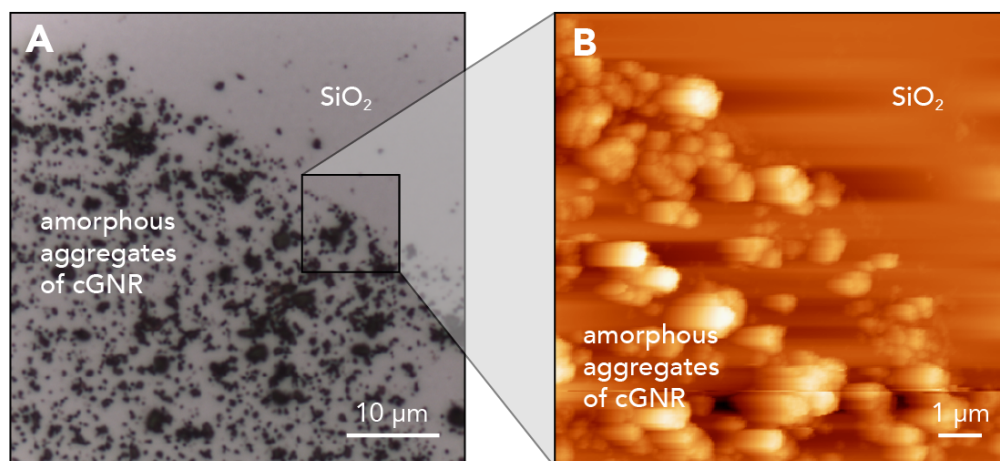


Figure S5. Negative Control Experiments for cGNR-COF Growth, related to Figure 2B

(A) Optical microscope image of a SiO₂ substrate after scooping the liquid-liquid interface of a negative control experiment with unfunctionalized cGNRs (cGNRs without aldehyde functional groups lining the edges).

(B) Ambient AFM image of the same region of the substrate. While the surface is covered with large amorphous cGNR aggregates collecting at the liquid-liquid interface no crystalline film boundary can be observed in the sample.

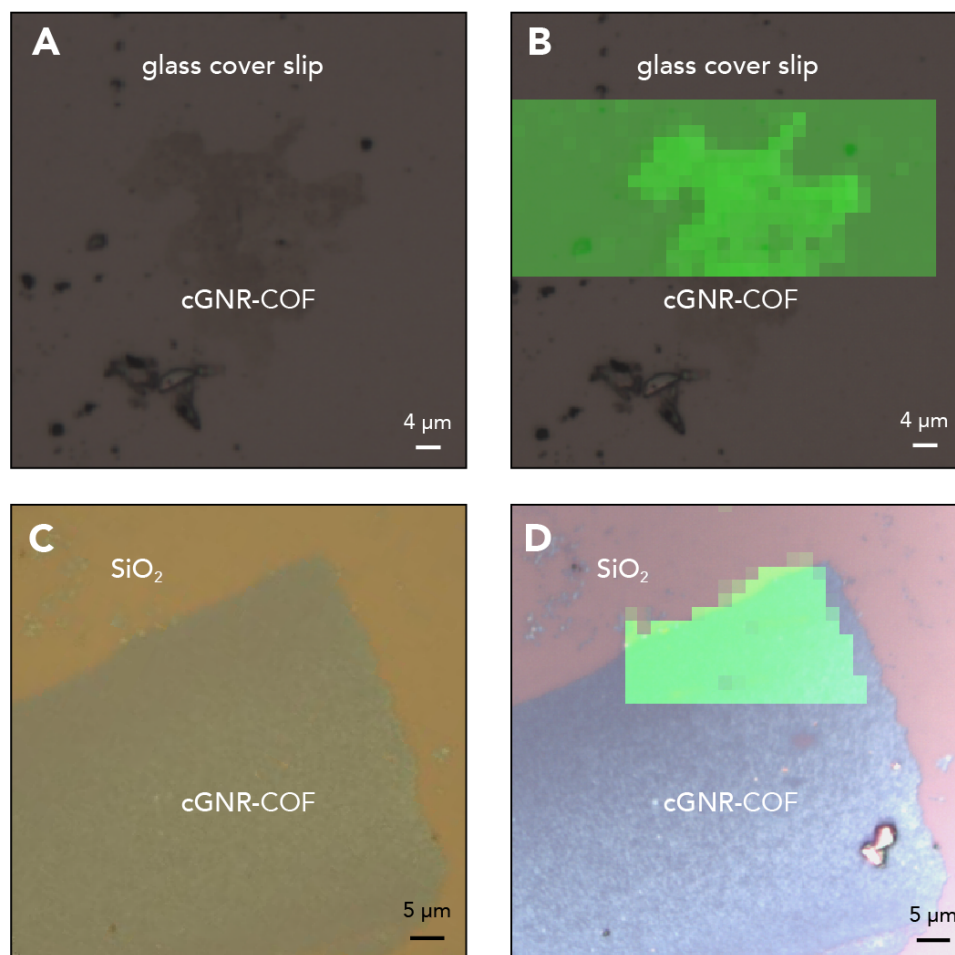


Figure S6. Spatial Raman Maps of the G-peak Intensity of cGNR-COFs on Si/SiO₂, related to Figure 2C

- (A) Optical microscope images of a cGNR-COF thin films on a glass slide.
- (B) Raman map of G-peak intensity overlaid on the microscope image in (A).
- (C) Optical microscope images of a cGNR-COF thin films on Si/SiO₂.
- (D) Raman map of G-peak intensity overlaid on the microscope image in (C).

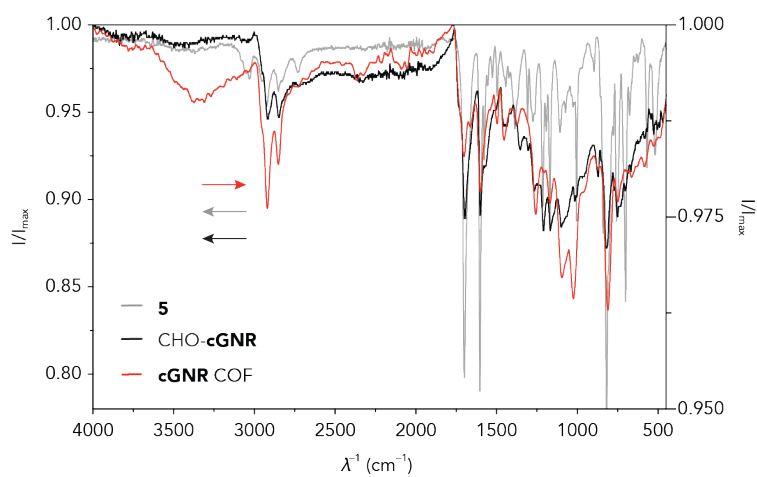


Figure S7. Expanded IR Spectrum of Poly-phenylene 5, CHO-cGNRs, and cGNR-COF, related to Figure 1E

FT-IR spectrum of 5 (gray), CHO-cGNRs (black), and cGNR-COF (red).

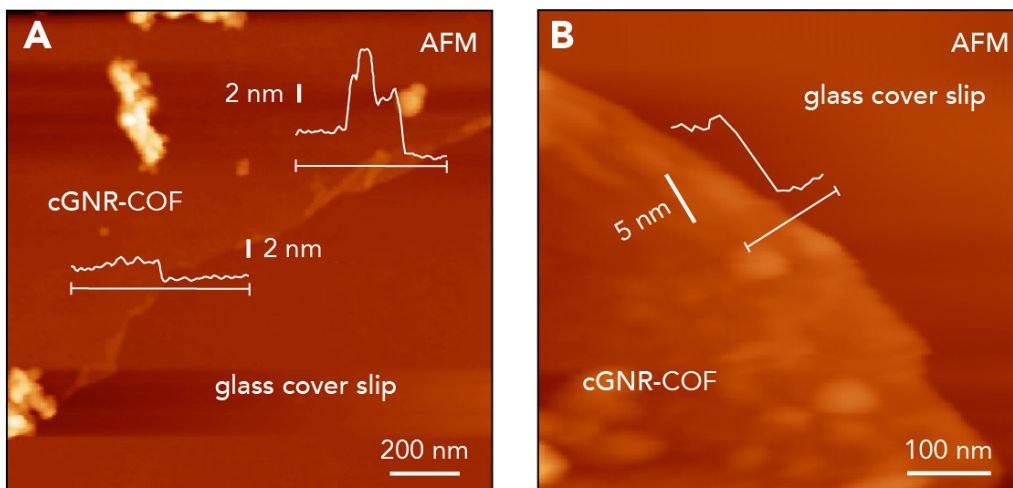


Figure S8. AFM Height Profiles of cGNR-COF Films, related to Figure 2E

(A) Ambient AFM of cGNR-COF film on a glass cover slip showing homogenous film thickness of ~2 nm.

(B) Ambient AFM of cGNR-COF film on HOPG showing homogenous film thickness of ~8 nm.

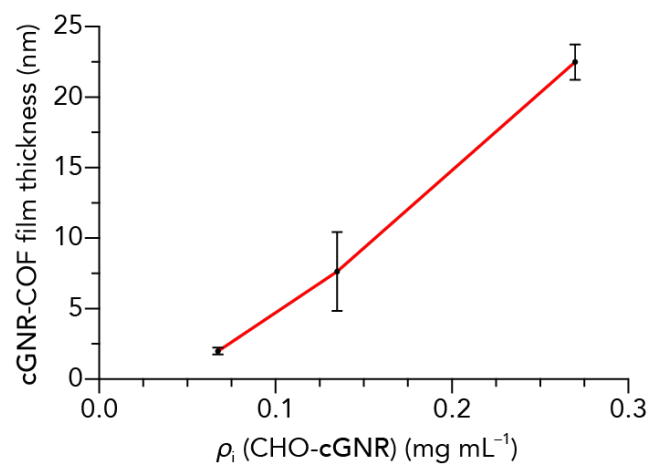


Figure S9. cGNR-COF Film Thickness as a Function of CHO-cGNRs in the Growth Solution
cGNR-COF film thickness as a function of CHO-cGNR mass concentration (ρ_i); film thicknesses were determined after transfer using ambient AFM.

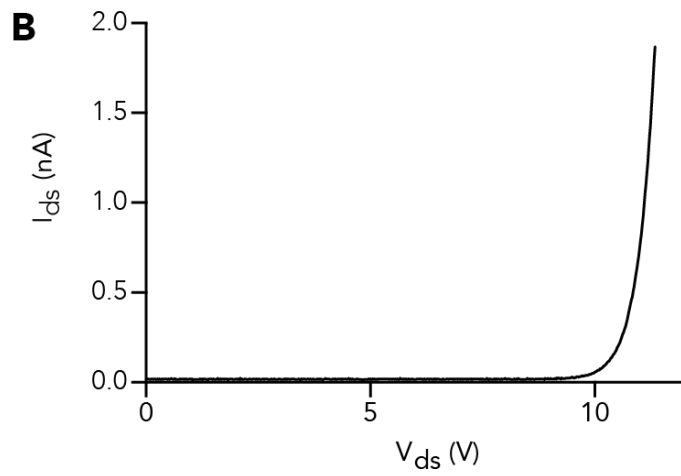
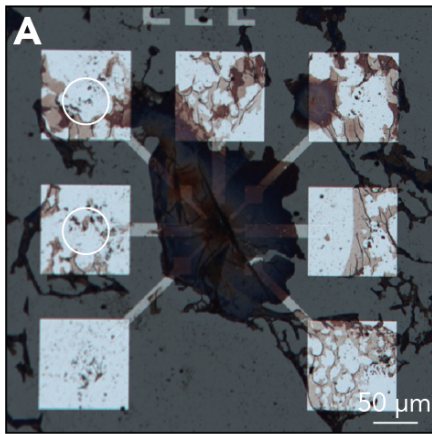


Figure S10. Electrical Characterization of cGNR-COF Thin Film Devices

(A) Optical microscope image of large-area, thick cGNR-COF film. White circles denote locations where the two-terminal measurements were performed.

(B) The I - V output characteristic curve shows a current onset around $V_{ds} = 10$ V at zero back-gate voltage ($V_g = 0$ V).

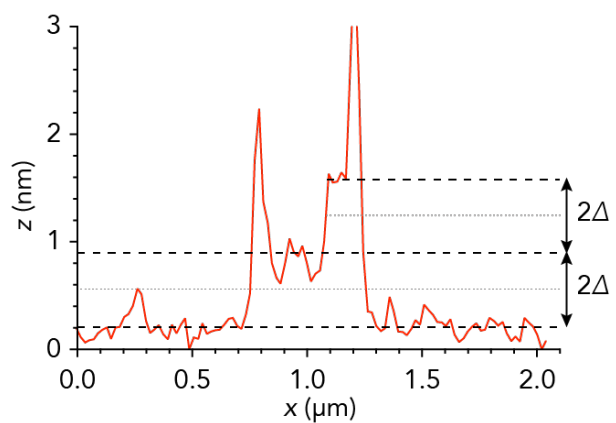


Figure S11. AFM Topographic Height Profile of a Tetralayer cGNR-COF flake on SiO₂, related to Figure 4

AFM topographic trace of liquid-phase exfoliated cGNR-COF on SiO₂. z-height profile shows a step-edge transition from a bilayer to a tetralayer flake.

Table S1. Structural Model for cGNR-COF

cGNR-COF			
Triclinic, $P\bar{1}$ $a = 5.0000 \text{ \AA}$, $b = 7.4000 \text{ \AA}$, $c = 25.5000 \text{ \AA}$ $\alpha = 100^\circ$, $\beta = 90^\circ$, $\gamma = 90^\circ$			
Atom	x	y	z
C1	0.29413	0.20248	0.04067
C2	0.09533	0.24133	0.08105
C3	0.27601	-0.11706	0.04717
C4	0.07798	-0.07794	0.08740
C5	0.98279	0.10117	0.10535
C6	0.39157	0.02162	0.02217
C7	0.66520	0.28812	0.16958
N8	0.77595	0.13195	0.14724
C9	0.41257	-0.21965	0.41913
C10	0.20870	-0.19678	0.45897
C11	0.51459	0.26045	0.39936
C12	0.10312	0.31701	0.47982
C13	0.71691	0.24226	0.35975
C14	0.14755	-0.49083	0.27373
C15	0.34666	-0.51776	0.23359
C16	0.40930	0.10956	0.41977
C17	0.20532	0.13903	0.45962
C18	0.51633	-0.39740	0.39895
C19	0.10143	-0.34471	0.48017
C20	0.71948	-0.43134	0.35908
C21	0.14582	0.18477	0.27476
C22	0.34612	0.15797	0.23440
C23	0.45061	0.30667	0.21290
C24	0.82310	0.39154	0.33881
C25	1.04090	0.36140	0.29548
C26	0.59240	-0.44461	0.57963
C27	0.79415	-0.46851	0.54017
C28	0.49465	0.07002	0.59898
C29	0.89539	0.01188	0.52069
H30	0.38160	0.31833	1.02185
H31	1.02333	0.38825	0.09448
H32	0.34191	-0.26594	0.03505
H33	-0.00948	-0.19354	0.10634
H34	0.72846	0.42199	0.15681

H35	1.06905	-0.34692	0.28936
H36	0.42831	-0.39551	0.21691
H37	0.06465	0.06242	0.29146
H38	0.42528	0.01419	0.21883
H39	0.80250	0.10116	0.34310
H40	0.80779	-0.31253	0.34171

II. Supplemental Experimental Procedures

Materials and Methods

Unless otherwise stated, all manipulations of air and/or moisture sensitive compounds were carried out in oven-dried glassware, under an atmosphere of N₂ or Ar. All solvents and reagents were purchased from Alfa Aesar, Spectrum Chemicals, Acros Organics, TCI America, and Sigma-Aldrich and were used as received unless otherwise noted. Organic solvents were dried by passing through a column of alumina and were degassed by vigorous bubbling of N₂ or Ar through the solvent for 20 min. Flash column chromatography was performed on SiliCycle silica gel (particle size 40–63 μm). Thin layer chromatography was performed using SiliCycle silica gel 60 Å F-254 pre-coated plates (0.25 mm thick) and visualized by UV absorption. HOPG substrates were purchased from SPI supplies (3 mm Grade SPI-3). All ¹H and ¹³C NMR spectra were recorded on Bruker AV-300, AVB-400, AV-600, DRX-500, and AV-500 MHz spectrometers, and are referenced to residual solvent peaks (CDCl₃ ¹H NMR = 7.26 ppm, ¹³C NMR = 77.16 ppm; CD₂Cl₂ ¹H NMR = 5.32 ppm, ¹³C NMR = 53.84 ppm). ESI mass spectrometry was performed on a Finnigan LTQFT (Thermo) spectrometer in positive ionization mode. MALDI mass spectrometry was performed on a Voyager-DE PRO (Applied Biosystems Voyager System 6322) in positive mode using a matrix of dithranol. Gel permeation chromatography (GPC) was carried out on a LC/MS Agilent 1260 Infinity set up with a guard and two Agilent Polypore 300 × 7.5 mm columns at 35 °C. All GPC analyses were performed on a 0.2 mg mL⁻¹ solution of polymer in CHCl₃. An injection volume of 25 μL and a flow rate of 1 mL min⁻¹ were used. Calibration was based on narrow polydispersity polystyrene standards ranging from M_w = 100 to 4,068,981 au. Raman spectroscopy was performed on a Horiba Jobin Yvon LabRAM ARAMIS confocal Raman microscope with 532 nm excitation wavelength. Wide-angle X-ray scattering (WAXS) data was acquired on beamline 7.3.3 at the Advanced Light Source with a Pilatus 2M detector. Powder samples were dropcast from acetone, dried in quartz capillaries and put into a helium atmosphere for measurement in transmission geometry. Silver behenate was used for calibration. The Nika package for IGOR Pro (Wavemetrics) was used to reduce the acquired 2D raw data to a 1D profile.¹ SEM was performed on a Zeiss Gemini Ultra-55 FESEM with an accelerating voltage between 2–10 kV. Low-dose HR-TEM images were acquired on the TEAM I instrument at the National Center for Electron Microscopy at the Molecular Foundry. TEAM I is an FEI Titan-class microscope operated at 300 kV, with geometric aberrations corrected to third order (with partial correction to fifth order) and chromatic aberrations corrected to the first order. Imaging data were collected at 24 °C with the Gatan K2 direct-detection camera operated in electron-counting mode. Images were recorded with total doses of 100 eÅ⁻² to minimize sample damage. SEM and TEM samples were prepared via scooping films directly, or drop-casting film dispersions onto lacey carbon TEM grids purchased from Ted Pella. Infrared spectroscopy was conducted with a Bruker ALPHA ATR-FTIR. ATR-FTIR samples were prepared by scooping thick films directly onto aluminum foil. UV-Vis spectroscopic measurements were conducted on a Varian Cary 50 spectrophotometer. All electrical measurements were performed under vacuum (2.8 e-8 Torr) at 24 °C using a Lakeshore TTPX probe station. 2,5-bis(4-bromophenyl)-3-phenyl-4-(3-((triisopropylsilyl)ethynyl)phenyl)cyclopenta-2,4-dien-1-one,² 2-(4-bromophenyl)-1,3-dioxolane³ and unfunctionalized cGNRs² were synthesized following literature procedures.

3-phenyl-2,5-bis(4-(4,4,5,5-tetramethyl-1,3,2-dioxaborolan-2-yl)phenyl)-4-(3-((triisopropylsilyl)ethynyl)phenyl)cyclopenta-2,4-dien-1-one (1) An oven dried 200 mL Schlenk flask with reflux condenser was charged under N₂ with 2,5-bis(4-bromophenyl)-3-phenyl-4-(3-((triisopropylsilyl)ethynyl)phenyl)cyclopenta-2,4-dien-1-one (0.50 g, 0.69 mmol), Pd(dppf)Cl₂ (91 mg, 0.11 mmol), anhydrous KOAc (0.67 g, 6.80 mmol), and bis(pinacolato)diboron (0.68 g, 2.68 mmol) in anhydrous dioxane (80 mL). The reaction mixture was stirred for 5 h at 95 °C. The solvent was removed and the crude product was redissolved in CH₂Cl₂, washed with H₂O, saturated aqueous NaCl solution, dried over Na₂SO₄, and concentrated on a rotary evaporator. The crude product was passed through a plug of silica (EtOAc). The solvent was removed and the solid was sonicated in MeOH. This process was repeated until the MeOH filtrate was colorless, yielding **1** (0.47 g, 0.58 mmol, 84%) as a purple solid. ¹H NMR (400 MHz, CDCl₃, 22 °C) δ = 7.67–7.59 (m, 4H), 7.33 (dt, *J* = 7.7, 1.4, 1H), 7.29–7.18 (m, 7H), 7.13 (t, *J* = 7.7, 1H), 6.97–6.90 (m, 4H), 1.31 (m, 24H), 1.05 (m, 21H) ppm; ¹³C {¹H} NMR (151 MHz, CD₂Cl₂, 22 °C) δ = 200.2, 155.8, 154.6, 134.8, 134.7, 134.2, 134.0, 133.7, 133.6, 133.5, 132.2, 129.9, 129.9, 129.8, 129.7, 129.3, 128.7, 128.6, 126.5, 126.1, 123.8, 106.9, 92.0, 84.4, 25.2, 19.0, 11.8 ppm; HRMS (ESI-TOF) *m/z*: [C₅₂H₆₂B₂O₅Si]⁺ calcd. [C₅₂H₆₂B₂O₅Si] 816.4547; found 816.4523.

2,5-bis(4'-(1,3-dioxolan-2-yl)-[1,1'-biphenyl]-4-yl)-3-phenyl-4-(3-((triisopropylsilyl)ethynyl)phenyl)cyclopenta-2,4-dien-1-one (2) A 25 mL Schlenk flask was charged with **1** (264 mg, 0.32 mmol), 2-(4-bromophenyl)-1,3-dioxolane(**2**) (224 mg, 0.98 mmol), and Aliquat 336 (6 drops) in 2M K₂CO₃ (3 mL) and dioxane (6 mL). The suspension was degassed via N₂ sparging for 30 min, after which Pd(PPh₃)₄ (60.4 mg, 0.053 mmol) was added under N₂. The reaction mixture was stirred at 100 °C for 20 h under N₂. The solution was cooled to 24 °C and diluted with CH₂Cl₂. The organic phase was washed with H₂O, saturated aqueous NaCl solution, dried over Na₂SO₄, and concentrated on a rotary evaporator. Column chromatography (SiO₂; 1–10% EtOAc/CH₂Cl₂) yielded **2** (189 mg, 0.22 mmol, 68%) as a purple solid. ¹H NMR (600 MHz, CDCl₃, 22 °C) δ = 7.64–7.60 (m, 4H), 7.56–7.50 (m, 8H), 7.37–7.33 (m, 5H), 7.31–7.28 (m, 1H), 7.27–7.23 (m, 2H), 7.17 (t, *J* = 7.7, 1H), 7.04–6.98 (m, 4H), 5.81–5.80 (m, 2H), 4.14–4.10 (m, 4H), 4.04–4.01 (m, 4H), 1.06–1.04 (m, 21H) ppm; ¹³C {¹H} NMR (101 MHz, CD₂Cl₂, 22 °C) δ = 200.7, 155.4, 154.2, 141.8, 141.8, 140.3, 140.1, 138.0, 133.8, 133.6, 133.6, 132.2, 131.1, 130.6, 130.4, 129.9, 129.7, 129.3, 128.7, 128.7, 127.6, 127.5, 127.4, 127.3, 127.3, 127.2, 125.9, 125.5, 123.8, 106.8, 104.0, 92.0, 65.9, 18.9, 11.8 ppm; HRMS (ESI-TOF) *m/z*: [C₅₈H₅₆O₅Si]⁺ calcd. [C₅₈H₅₆O₅Si] 860.3892; found 860.3891.

2,5-bis(4'-(1,3-dioxolan-2-yl)-[1,1'-biphenyl]-4-yl)-3-(3-ethynylphenyl)-4-phenylcyclopenta-2,4-dien-1-one (3) An oven dried 25 mL Schlenk flask was charged under N₂ with **2** (61.3 mg, 0.07 mmol) in anhydrous THF (7 mL). A solution of TBAF (0.76 mL, 0.076 mmol, 0.1 M in THF) was added dropwise to the solution over a period of 5 min at 24 °C. The solution was stirred for an additional 10 min and the reaction was quenched with H₂O. The suspension was extracted with CH₂Cl₂ and the organic phase was washed with H₂O, dried over Na₂SO₄ and concentrated on a rotary evaporator. Column chromatography (SiO₂; 3:2 hexanes/EtOAc) yielded **3** (23.9 mg, 0.034 mmol, 48%) as a purple solid. ¹H NMR (500 MHz, CD₂Cl₂, 22 °C) δ = 7.64–7.60 (m, 4H), 7.56–7.50 (m, 8H), 7.41 (dt, *J* = 7.7, 1.2, 1H), 7.35–7.32 (m, 4H), 7.31–7.29 (m, 1H), 7.26–7.18 (m, 3H), 7.14–7.12 (m, 1H), 7.03–6.99 (m, 3H), 5.81–5.80 (m, 2H), 4.14–4.11 (m, 4H), 4.04–4.00 (m, 4H), 3.06 (s, 1H) ppm; ¹³C {¹H} NMR (101 MHz, CD₂Cl₂, 22 °C) δ = 200.7, 155.3, 154.2, 141.8, 141.8, 140.3, 140.1, 138.0, 138.0, 134.3, 133.5, 133.1, 132.7, 131.1, 130.6, 130.3, 130.3, 129.8, 129.3, 128.9, 128.7, 127.6, 127.4, 127.3, 127.3, 127.2, 126.0, 125.4, 122.6, 104.0, 83.3, 78.3, 65.9 ppm; HRMS (ESI-TOF) *m/z*: [C₄₉H₃₆O₅]⁺ calcd. [C₄₉H₃₆O₅] 704.2557; found 704.2558

poly-4 An oven dried 5 mL sealable tube was charged under N₂ with **3** (55.9 mg, 0.079 mmol) in Ph₂O (279.5 mg, 0.25 mL). The solution was degassed. The tube was sealed under N₂ and heated to 230 °C for

18 h. The solution was cooled to 24 °C, MeOH was added, and the precipitate was collected via centrifuge. The precipitate was dissolved in THF and reprecipitated with MeOH (1:2 THF/MeOH) and the resulting precipitate was collected via centrifuge. This process was repeated three times yielding **4** (46.8 mg, 87%) as a colorless solid. ¹H NMR (400 MHz, CD₂Cl₂, 22 °C) δ = 7.61–7.34 (m, 8H), 7.31–6.50 (m, 18H), 5.83–5.71 (br s, 2H), 4.16–3.89 (m, 8H)

poly-5 A 20 mL vial was charged with **4** (83.1 mg, 0.12 mmol) in CHCl₃ (9 mL) under N₂. At 24 °C a solution of p-TsOH·H₂O (17.1 mg, 0.09 mmol) in acetone (2 mL) was added dropwise. The solution was stirred at 24 °C for 24 h. The reaction was quenched with saturated NaHCO₃ and the organic phase was collected, washed with H₂O, saturated aqueous NaCl solution, and dried over MgSO₄. The combined organic phases were concentrated and the polymer was precipitated via addition of MeOH. The solid was collected via centrifuge and reprecipitated from THF:MeOH (1:2). The crude polymer (66 mg, 0.10 mmol, 93%) was further purified via preparative GPC (CHCl₃), yielding a colorless solid (25.5 mg, 0.04 mmol, 36%) ¹H NMR (400 MHz, CDCl₃, 22 °C) δ = 10.06–9.85 (m, 2H), 7.94–7.29 (m, 10H), 7.21–6.45 (m, 16H) ppm

CHO-cGNR An oven dried 250 mL Schlenk flask was charged under N₂ with **5** (21.6 mg, 0.037 mmol) in anhydrous CH₂Cl₂ (120 mL). While sparging with N₂, a solution of FeCl₃ (352.2 mg, 2.17 mmol, 7 eq. per H) in anhydrous MeNO₂ (3.5 mL) was added at 0 °C. The reaction mixture was warmed to 24 °C and stirred for 72 h under a continuous stream of N₂. The black reaction mixture was quenched with MeOH and filtered over a membrane filter. The precipitate was washed with MeOH and THF. The solid was sonicated in (1:1) toluene/THF, filtered, then washed with THF, acetone, hexanes, ethyl acetate, and acetone yielding a dark purple precipitate CHO-cGNR (21.5 mg, 99%). Raman (powder) λ⁻¹ = 253, 1277, 1332, 1603, 2688, 2892, 2942, 3216 cm⁻¹

cGNR-COF thin films A dispersion of CHO-cGNR (1.349 mg) in (1:1) *o*-DCB/CHCl₃ (4 mL), was added to a solution of benzidine (0.431 mg, 0.002 mmol) in (1:1) *o*-DCB/CHCl₃ (1 mL) and filtered through a pad of glass wool. A silanized vial was charged with the reaction mixture and carefully layered with a 5 mM Sc(OTf)₃ (aq.) solution. The vial was left undisturbed for 7 days, during which a gray film began to appear at the interface of the two liquids. The aqueous phase was gently removed by syringe and replaced with H₂O. The organic phase was gently removed and replaced with (1:1) *o*-DCB/CHCl₃. The film formed at the interface was scooped onto a substrate. The film was washed by dipping the substrate into water, acetone then isopropyl alcohol.

cGNR-COF film powder A dispersion of CHO-cGNR (1.349 mg) in (1:1) *o*-DCB/CHCl₃ (4 mL), was added to a solution of benzidine (0.431 mg, 0.002 mmol) in (1:1) *o*-DCB/CHCl₃ (1 mL) and filtered through a pad of glass wool. A silanized vial was charged with the reaction mixture and carefully layered with a 5 mM Sc(OTf)₃ (aq.) solution. The vial was left undisturbed for 7 days, during which a gray film began to appear at the interface of the two liquids. The aqueous phase was gently removed by syringe and replaced with H₂O. The organic phase was gently removed and replaced with (1:1) *o*-DCB/CHCl₃. A maximum amount of aqueous and organic phase was removed without disturbing the film. The interface suspended film was quickly poured into an excess of acetone. The film suspension was allowed to settle and the majority of the acetone was removed and replaced with fresh acetone. This process was repeated four times and the film dispersion were stored in acetone.

Liquid-phase exfoliation of cGNR-COF films A dispersion of cGNR-COF films in acetone (2–3 drops) was added to *o*-DCB (1 mL) and the suspension was sonicated for 15 min. The resulting dispersion was drop-

cast onto the desired substrate at 24 °C and the solvent was removed under a stream of N₂. The substrate was gently rinsed with water, acetone, isopropyl alcohol, and dried under a stream of N₂.

III. Supplemental References

1. Ilavsky, J.N. (2012). Software for Two-Dimensional Data Reduction. *J. Appl. Crystallogr.* *45*, 324–328.
2. Rogers, C., Perkins, W.S., Veber, G., Williams, T.E., Cloke, R.R., and Fischer, F.R. (2017). Synergistic Enhancement of Electrocatalytic CO₂ Reduction with Gold Nanoparticles Embedded in Functional Graphene Nanoribbon Composite Electrodes. *J. Am. Chem. Soc.* *139*, 4052–4061.
3. Wang, B., Li, P., Yu, F., Chen, J., Qu, Z., Han, K. (2013). A near-infrared reversible and ratiometric fluorescent probe based on Se-BODIPY for the redox cycle mediated by hypobromous acid and hydrogen sulfide in living cells. *Chem. Commun.* *49*, 5790.